ASCE

Performance of Various Geosynthetic-Reinforced Embankment and Foundation Systems Subjected to Reverse Fault Movement

Jung Chiang[1]; Chun-Wei Wu[2]; Kuo-Hsin Yang[3]; Yuan-Chun Chung[4]; and B. V. S. Viswanadham[5]

Abstract: This paper presents reduced model tests on geosynthetic-reinforced soil (GRS) embankment and foundation systems subjected to reverse fault movements. Three types of reinforced foundations—soil foundations reinforced with planar geotextiles, geosynthetic encased granular columns (GECs), and geocells—were examined to investigate the effectiveness and reinforcing mechanisms in mitigating reverse fault-induced ground deformation. Digital image analysis (DIA) techniques were adopted to evaluate the surface displacement profiles, maximum angular distortion (β_{max}), and shear strain contours at different magnitudes of reverse fault displacement. The maximum horizontal facing displacement (Δ_{max}) of the overlying GRS embankment was also determined to evaluate the overall performance of the GRS embankment and foundation systems. Test results indicated that different reinforcing mechanisms and the development of fault-induced shear ruptures were observed for three types of reinforced foundations. The geocell foundation had the most optimal effects in minimizing the β_{max} at the ground surface, as well as the Δ_{max} of the GRS embankment. Compared with the unreinforced foundation, a reduction of 39.1% in the Δ_{max} value of the GRS embankment was observed at a fault movement to foundation thickness ratio (S/H_F) of 37.5%. For all the reinforced embankment and foundation systems, the overlying GRS embankment remained stable, and only localized deformation on the wrapped-around facing was observed. The influence of overburden pressure applied by the GRS embankment on the performance of each reinforced foundation, as well as the design implications of the embankment and foundation systems, were discussed in the present study.
DOI: 10.1061/JGGEFK.GTENG-12785.

Author keywords: Geosynthetic; Geosynthetic encased granular column (GEC); Geocell; Reverse fault; Angular distortion.

Introduction

Distinct surface ruptures are recognized as a critical hazard associated with earthquake fault movements. Severe ground surface deformation could result in extensive damage to buildings or infrastructure located on active fault zones. Generally, construction across active faults should be avoided. Regulations have imposed restrictions on the construction of buildings within fault setback areas. However, avoidance is often challenging for linear infrastructure such as highway and railway embankments. In such scenarios, flexible and resilient earth structures, such as geosynthetic-reinforced soil (GRS) structures, can effectively mitigate the effects of fault-induced ground deformation and differential settlement (Delli Carpini et al. 2024; Ahmadi and Fadaee 2023; Al Heib et al. 2021; Rasouli and Fatahi 2021; Ardah et al. 2018; Moosavi and Jafari 2012).

GRS structures are implemented in engineering practice to mitigate surface fault hazards. An iconic project, which involved a GRS highway embankment across the Chelungpu active fault (Fig. 1), was carried out in central Taiwan. In the 1999 Chi-Chi earthquake ($M_L = 7.3$), a rigid gravity retaining wall across the Chelungpu fault experienced collapse due to ground surface deformation resulting from the fault movement. The average vertical displacement measured at the ground surface in the Chi-Chi earthquake was 2–4 m (Chen et al. 2001). This incident led to the adoption of a relatively flexible GRS embankment and foundation system across the Chelungpu fault to reduce the risk of embankment collapse due to fault-induced ground deformation. This reinforced system comprises a GRS embankment overlying a reinforced foundation. The function of the GRS embankment was to accommodate differential settlement and preserve the stability and serviceability of the embankment, while the reinforced foundation was designed to limit fault-induced angular distortion to an acceptable extent.

Studies have demonstrated that increasing the ductility of the soil layers overlying bedrock faults can prevent fault-induced ground deformation to a certain degree (Bray and Garcia 2022; Garcia and Bray 2018; Ashtiani et al. 2018; Oettle and Bray 2013; Anastasopoulos et al. 2007; Bray 2001, 2009; Lazarte and Bray 1996; Lazarte et al. 1994; Bray et al. 1993). Specifically, a compacted soil layer reinforced by planar reinforcements (referred to as a GRS foundation in this paper) may be the most viable and cost-effective option to enhance the ductility of the soil layers overlying a bedrock fault. Yang et al. (2020) explored the performance of GRS

[1]Postdoctoral Fellow, Dept. of Civil Engineering, National Taiwan Univ., 1, Sec. 4, Roosevelt Rd., Taipei 106, Taiwan. Email: jungchiang@ntu.edu.tw

[2]Ph.D. Student, Dept. of Civil Engineering, National Taiwan Univ., 1, Sec. 4, Roosevelt Rd., Taipei 106, Taiwan. Email: f10521108@ntu.edu.tw

[3]Professor, Dept. of Civil Engineering, National Taiwan Univ., 1, Sec. 4, Roosevelt Rd., Taipei 106, Taiwan (corresponding author). ORCID: https://orcid.org/0000-0003-4460-7085. Email: khyang@ntu.edu.tw

[4]Graduate Student, Dept. of Civil Engineering, National Taiwan Univ., 1, Sec. 4, Roosevelt Rd., Taipei 106, Taiwan. Email: r11521110@ntu.edu.tw

[5]Professor, Dept. of Civil Engineering, Indian Institute of Technology Bombay, Powai, Mumbai, Maharashtra 400 076, India. Email: viswam@civil.iitb.ac.in

Note. This manuscript was submitted on March 5, 2024; approved on October 25, 2024; published online on February 13, 2025. Discussion period open until July 13, 2025; separate discussions must be submitted for individual papers. This paper is part of the ***Journal of Geotechnical and Geoenvironmental Engineering***, © ASCE, ISSN 1090-0241.

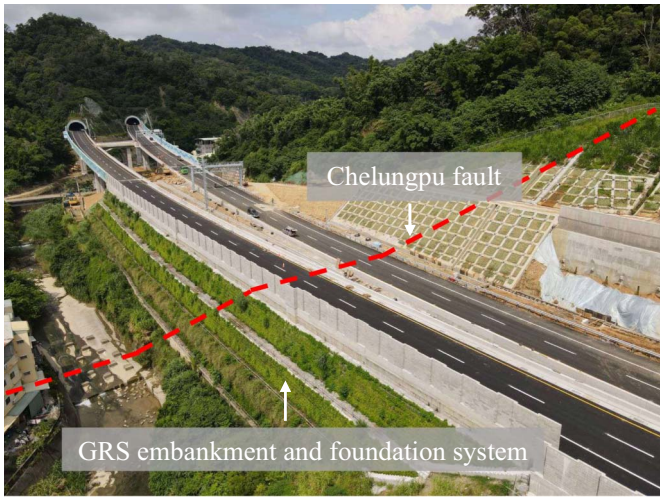

Fig. 1. Reinforced system constructed in central Taiwan to mitigate hazards associated with surface fault rupture. (Image by authors.)

foundations under normal faulting conditions through a series of reduced model tests. The test results revealed that the GRS foundations reduced fault-induced angular distortion at ground surface level by 60% in comparison with unreinforced compacted soil layers. In addition, the fault-induced shear rupture was intercepted by the reinforcements and spread over a relatively wide influential fault zone, resulting in a gentle ground surface deformation profile. Although the efficacy of GRS foundations in mitigating normal fault-induced ground deformation has been well-documented, there are few studies that explore their performance under reverse faulting conditions. Furthermore, GRS foundations may be ineffective in reducing ground deformation induced by reverse fault movement because tensile force is not expected to develop in planar reinforcements given that a GRS foundation is primarily subjected to compression as the hanging wall moves toward the footwall. Other types of reinforced foundations, soil foundations reinforced by geosynthetic encased granular columns (GECs) and geocells, which provide bending stiffness against compressive forces induced by bending deformation, may be able to overcome the aforementioned deficiencies; thus, these types of reinforced foundations were assessed in the present study.

Geosynthetic encased granular columns are commonly used to support highway embankments that overlie weak cohesive subgrade soils. Experimental and numerical studies have revealed that GECs can provide sufficient vertical support to embankments and can enhance the load-bearing capacity of subgrade soils (Abid et al. 2022; Rathod et al. 2021; Chen et al. 2018; Gu et al. 2017; Hasan and Samadhiya 2017; Hong et al. 2016; Almeida et al. 2014; Chen et al. 2015; Hosseinpour et al. 2015). Studies have also evaluated the performance of GECs under shear loading conditions and the benefits of using GECs to provide lateral resistance in slope stabilization (Zhang et al. 2022; Hajiazizi et al. 2020; Cengiz et al. 2019; Hajiazizi et al. 2018; Zhang and Wang 2017; Gu et al. 2016; Mohapatra et al. 2016). These studies have demonstrated that encasing granular columns with geotextile can significantly enhance shear and bending resistances, thereby improving overall performance under shear loading.

Similarly, geocells have been used in the foundations of highway embankments to increase the bearing capacity of subgrade soils. Studies have reported that geocells can provide high confinement to infilled soils and increase the soil shear strength while distributing the imposed stress over a relatively wide area in the lateral direction (Yin et al. 2024; Khan et al. 2023; Ari and Misir 2021; Gedela et al. 2021; Mehdipour et al. 2013; Thallak et al. 2007; Biabani et al. 2016; Hegde and Sitharam 2015). Furthermore, unlike the planar reinforcement embedded in GRS foundations, the three-dimensional geocell-soil composite provides bending resistance, which can constrain the deformation of the surrounding soil (Khorsandiardebili and Ghazavi 2021; Zhang et al. 2018; Mehdipour et al. 2013; Tang and Yang 2013; Pokharel et al. 2010). Although related studies have validated the benefits of using GEC and geocell foundations to increase the bearing capacity of subsoils, the performance of GEC and geocell foundations in mitigating fault-induced ground deformation has yet to be fully understood. Furthermore, no study has investigated the performance or mechanical behaviors of reinforced embankment and foundation systems against reverse fault movement.

To fill the identified research gaps, this study carried out a series of reduced model tests on three types of reinforced foundations: GRS, GEC, and geocell foundations. For comparison purposes, a reduced model test was also conducted on an unreinforced foundation. The effectiveness and reinforcing mechanisms of GRS, GEC, and geocell foundations in minimizing ground surface deformation due to reverse faulting were studied. The reduced model tests, based on relevant scaling laws, simulated 3-m-thick prototype reinforced foundations subjected to reverse fault displacements reaching up to 1.12 m. Digital image analysis (DIA) techniques were adopted to evaluate the surface displacement profile, maximum angular distortion, and shear strain contours at different magnitudes of reverse fault displacement. Furthermore, another series of reduced model tests were conducted on the reinforced embankment and foundation systems comprising a GRS embankment overlying the unreinforced foundations and reinforced foundations (i.e., GRS, GEC, and geocell foundations) to investigate the overall performance of the reinforced systems against reverse fault movement. Each of the reduced models simulated a 1.8-m-high GRS embankment in prototype constructed on a reinforced foundation. The maximum horizontal displacement of the GRS embankment facing was determined to evaluate the stability of the embankment. This study primarily aimed to (1) evaluate the effectiveness of the GRS, GEC, and geocell foundations; (2) investigate the reinforcing mechanisms of the reinforced foundations; and (3) evaluate the overall stability of the reinforced embankment and foundation systems against reverse fault movement. Design implications for reinforced embankment and foundation systems are discussed in this paper on the basis of the findings of this study.

Reduced Model Tests

Reduced Scale Model and Test Program

In this study, the reduced model tests were conducted with the use of a sandbox in the geotechnical research laboratory at National Taiwan University. Fig. 2 shows a schematic of the sandbox and the experimental setup. The dimensions of the sandbox were $1.06 \times 0.21 \times 0.60$ m (length × width × height). The front wall of the sandbox was made of transparent plexiglass to enable visual observation during testing. To ensure that the models were tested under plane strain conditions, lubricant sandwiched between two thin PE sheets was attached to both sides of the plexiglass walls of the sandbox to minimize the soil-wall interface friction. Liu et al. (2014) have quantified the effect of interface treatments on reducing interface friction by conducting large-scale direct shear tests. Test results indicated that lubricant sandwiched between PE sheets could reduce up to 80% of interface friction. The bottom of the

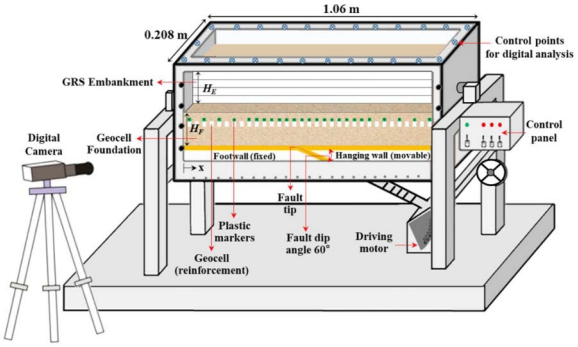

(a)

(b)

Fig. 2. Sandbox and reduced model test setup: (a) illustration; and (b) panorama.

sandbox consisted of a movable hanging wall and a fixed footwall. A driving motor was installed underneath the hanging wall [see Fig. 2(a)] to generate reverse fault displacement by moving the hanging wall upward. The fault tip was initially located at $x =$ 58 cm from the left boundary, and a fault dip angle of 60° was examined in the study.

Reduced model tests were first conducted on the unreinforced foundation and the three types of reinforced foundations (i.e., GRS, GEC, and geocell foundations). The dimensions of the prototype foundations were reduced by a factor of 15 in the reduced model tests (i.e., target scaling ratio $N = 15$) in accordance with the relevant scaling laws (to be discussed). Table 1 summarizes the testing program and design parameters for the reduced model tests. The abbreviation GRE shown in Table 1 stands for the overlying GRS embankment, while UF, GRF, GECF, and GCF stand for unreinforced, GRS, GEC, and geocell foundations, respectively. The height of both the unreinforced and reinforced foundations was $H_F = 20$ cm, corresponding to 3 m in the prototype. Fig. 3 presents images of the reinforcements and schematics of the GRS, GEC, and geocell foundation tests. Subsequently, a series of reduced model tests were conducted on the reinforced embankment and foundation systems. Fig. 4 shows a test model of the reinforced embankment and foundation systems. A 12-cm-high GRS embankment ($H_E = 12$ cm, corresponding to 1.8 m in the prototype) was constructed on each of the three reinforced foundations ($H_F = 20$ cm, corresponding to 3 m in the prototype). For comparison, a GRS embankment with an unreinforced foundation was also tested.

Material Properties

The soil material used in this study was quartz sand, which is classified as poorly graded sand (SP) in the Unified Soil Classification System (USCS). Fig. 5 shows the grain size distribution curve of the sand. Table 2 summarizes the material properties of the sand, which were determined on the basis of the American Society for Testing and Materials (ASTM) standards. In the present study, the foundations and overlying GRS embankment were constructed layer-by-layer at a target relative density of $D_r = 70\%$. The required weight for each soil layer was calculated based on a target dry unit weight (i.e., $\gamma_d = 15.3$ kN/m^3 at $D_r = 70\%$) and the volume of the soil layers. A known amount of sand was pluviated from a hopper into the sandbox at a specified drop height to achieve uniform density. This technique was utilized by Li et al. (2019) in reduced model tests to prepare fairly uniform sand deposits. Triaxial consolidated–drained compression tests [ASTM D7181 (ASTM 2015)] were conducted to determine the shear strength properties of the sand. The sand had an effective cohesion of $c' = 0$ kN/m^2 and an effective friction angle of $\phi' = 39°$.

The reinforcing material used was a nonwoven geotextile made of polypropylene. This material is not a commercial geotextile used in engineering practice; rather, it was originally designed for use in the inner lining of shoes. Table 2 shows the material properties of the nonwoven geotextile. The planar geotextile, geotextile encasement, and geocell placed in the GRS, GEC, and geocell foundations, respectively, were made from the same nonwoven geotextile, which was also used as the reinforcing material for the overlying GRS embankment. Wide-width tensile tests [ASTM D4595 (ASTM 2011)] were conducted to evaluate the tensile strength properties of the nonwoven geotextile. Fig. 6 presents the tensile test results for the nonwoven geotextile tested in the machine and cross-machine directions. The nonwoven geotextile exhibited an ultimate tensile strength of $T_{ult} = 0.7$ kN/m and a failure strain of $\varepsilon_f = 32.39\%$ in

Table 1. Experimental program of reduced model tests

Description	Test ID	Foundation height, H_F (cm)	GRS embankment height, H_E (cm)	Total area of foundation reinforcement, A_R (cm^2)
Unreinforced foundation	UF	20	—	—
GRS foundation	GRF	20	—	6,614
GEC foundation	GECF	20	—	2,545
Geocell foundation	GCF	20	—	6,336
GRS embankment with unreinforced foundation	GRE + UF	20	12	—
GRS embankment with GRS foundation	GRE + GRF	20	12	6,614
GRS embankment with GEC foundation	GRE + GECF	20	12	2,545
GRS embankment with geocell foundation	GRE + GCF	20	12	6,336

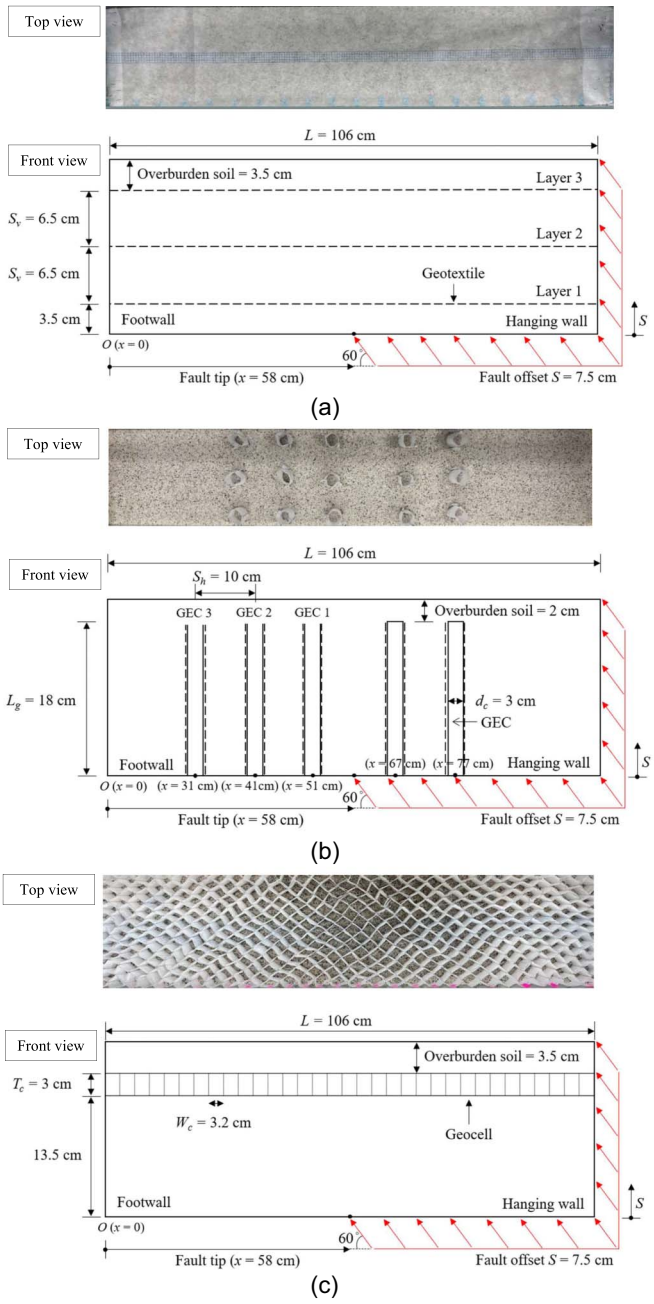

Fig. 3. Reinforced foundation tests (not in scale): (a) test GRF; (b) test GECF; and (c) test GCF.

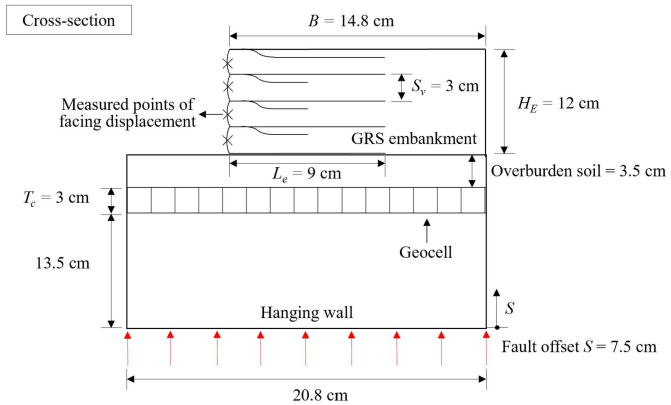

Fig. 4. Reinforced system tests (test GRE + GCF).

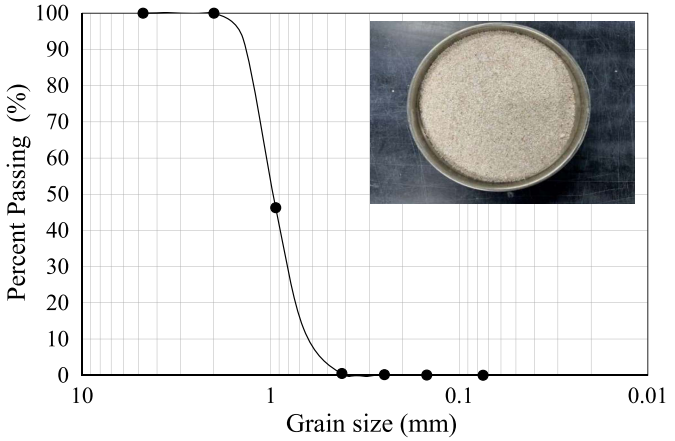

Fig. 5. Grain size distribution curve and the image of test sand.

Table 2. Properties of soil and reinforcement materials

Property	Value
Soil	
USCS soil classification	SP
Specific gravity, G_s	2.65
Mean particle size, D_{50} (mm)	0.98
Relative density, D_r (%)	70
Target dry unit weight, γ_d (kN/m^3)	15.3
Cohesion, c' (kPa)	0
Peak friction angle, ϕ' (degrees)	39
Reinforcement	
Material	Polypropylene (PP)
Mass per unit area (g/m^2)	29.6
Thickness (mm)	0.235
Ultimate tensile strength, T_{ult} (kN/m)	0.70
Ultimate tensile strain, ε_{ult} (%)	32.39
Stiffness, J_{50} (kN/m)	5.47
Joint ultimate tensile strength, T_j (kN/m)	1.75
Soil—Reinforcement interface	
Peak interface friction angle, δ' (degrees)	27.4
Efficiency factor, E_ϕ	0.63

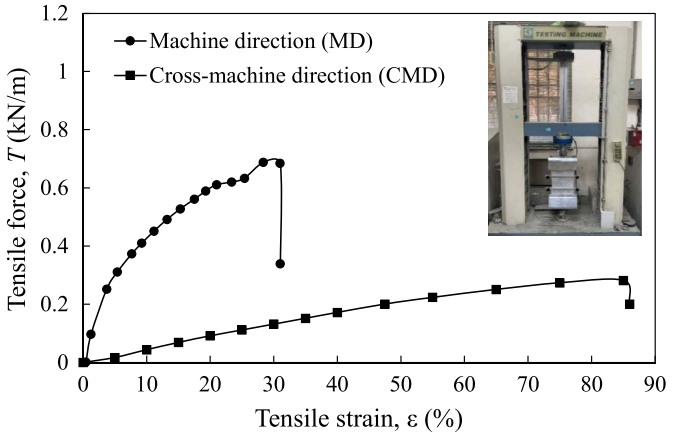

Fig. 6. Results of wide-width tensile tests for nonwoven geotextile.

the machine direction, with a tensile stiffness at half of the ultimate tensile strength being $J_{50} = 5.47$ kN/m. In the cross-machine direction, the ultimate tensile strength was $T_{ult} = 0.29$ kN/m, with a failure strain of $\varepsilon_f = 87.4\%$ and tensile stiffness of $J_{50} = 0.46$ kN/m.

In the GRS foundation tests, the machine direction of the geotextile was oriented perpendicular to the fault rupture to achieve high mobilized tensile force against reverse fault movement. For the geotextile encasement used in the GEC foundation tests, the machine direction of the geotextile was oriented along the circumferential direction of the GECs to achieve high hoop stress. For the fabrication of the geocells, tailored geotextile strips were firmly sewn to a cellular shape to provide high confinement to the infilled sand. The machine direction of the geotextile strips was oriented in the longitudinal direction of the geocells. The ultimate tensile strength of the joints was $T_j = 1.75$ kN/m, which was higher than that of the nonwoven geotextile (i.e., $T_{ult} = 0.7$ kN/m) to prevent failure at the seam. A similar approach was employed in past studies (Changizi et al. 2021; Rahimi et al. 2018; Tafreshi and Dawson 2010; Sitharam and Sireesh 2005) to prepare geocell materials in different scales of testing.

Model Preparation and Testing Procedures

In practice, reinforced foundations can extend over long distances and cover potential fault zones because fault-induced shear ruptures are often difficult to predict. Linear reinforced foundations can not only reduce fault-induced ground deformation but also enhance the bearing capacity of the foundation soils. This study focuses on reinforced foundations fully covered with planar geotextiles, GECs, and geocells, as shown in Figs. 3(a–c). The effects of the length and location of the planar geotextile, GEC, and geocell were not evaluated in the present study.

The GRS foundation was constructed by placing an initial sand layer followed by a planar geotextile. Specifically, three layers of the planar geotextile were installed in the GRS foundation with vertical spacing of $S_v = 6.5$ cm [Fig. 3(a)]. The planar geotextile was placed from the left boundary to the right boundary of the sandbox to simulate the field condition in which the reinforcement was embedded long enough in the soil beyond the influential fault zone. Regarding the GEC foundations, lubricated thin-walled steel tubes were used to construct the GECs. The sand in GECs was constructed using the volume control method to reach the target relative density (i.e., $D_r = 70\%$). The known quantity of sand was filled into the geotextile encasement layer-by-layer and carefully compacted to a specific height by a small-size compaction hammer. Once the GEC construction was finalized, the steel tubes were extracted from the soil layer with utmost care to minimize disturbance. A 1.5-cm-thick soil layer was then placed over the GEC foundations to provide adequate overburden pressure and avoid the pulling up of GECs during testing. The overlying soil layer has a minor effect on the performance of the GEC foundation in reducing fault-induced ground deformation since the thickness of the soil layer was relatively thin, compared with the foundation height (i.e., $H_F = 20$ cm). The configuration of the GECs was determined by considering the influential fault zone generated at the maximum fault displacement (i.e., $S = 7.5$ cm). The GECs featured a diameter of $d_c = 3$ cm, and the length of the GECs was $L_g = 18$ cm (yielding a length-to-diameter ratio of $L_g/d_c = 6$), as shown in Fig. 3(b). The horizontal spacing of the GECs was determined to be $S_h = 10$ cm on the basis of the reduced model test results reported by Chiang et al. (2023), which suggested that a GEC foundation with a GEC spacing-to-diameter ratio (S_h/d_c) of 3.3 yielded the most substantial reduction in maximum fault-induced angular distortion. Regarding the geocell foundation, a 3-cm-thick geocell was installed in this foundation [Fig. 3(c)]. The geocell had a square shape and a 3.2 cm × 3.2 cm aperture opening size. The geocell was filled with sand, which was then carefully compacted to the target relative density of 70%. A 3.5-cm-thick overburden soil layer was covered on the geocell layer to provide a buffer for proper compaction on the geocell layer and prevent geocell damage in the compaction.

Fig. 4 presents a schematic of the reduced model tests conducted on the reinforced embankment and foundation systems. For the test model of the GRS embankment, the configuration of the reinforcement was determined by following the conventional design of a GRS structure. Specifically, the reinforcement length was $L_e = 9$ cm ($L_e = 0.7H_E$), and the vertical spacing was $S_v = 3$ cm. The GRS embankment was constructed under a relative density of $D_r = 70\%$ to comply with prevailing design guidelines.

After the test models were constructed, the fault displacement was applied to the right and bottom boundaries of the hanging wall to simulate 60° dip reverse fault movement. The maximum fault displacement was up to $S = 7.5$ cm (i.e., $S = 1.12$ m in prototype scale), which was determined based on the fault displacement corresponding to a strong earthquake ($M_L = 6.0$-7.0) according to the U.S. Geological Survey (Bonilla 1967). A series of images was captured at $S = 1.5$, 3, 4.5, 6, and 7.5 cm to investigate the mechanical behaviors of the reinforced foundations and systems at multiple magnitudes of reverse fault displacement. The maximum ratio of fault displacement to the height of the foundations was $S/H_F = 37.5\%$.

Similitude Requirements

To ensure the comparable behaviors of the prototype and the test models, the similarity of the reduced model tests was carefully considered in the present study. Scaling factors derived from the Buckingham Pi Theorem (Buckingham 1914) were used to scale down the material properties for the reduced model tests. Table 3 provides a summary of these scaling factors along with the corresponding values for geometry and material properties. These scaling factors have also been employed in various studies (Yoo et al. 2022; Garcia et al. 2007; Yasuhara and Recio-Molina 2007; Viswanadham and Konig 2004) to account for the degree of similarity among reduced scaled models for GRS structures. On the basis of the relevant scaling factors, the tensile properties of the reinforcing material used in the reduced model tests were scaled down by a factor of N^2, where N is the target scaling ratio. A target scaling ratio of $N = 15$ was selected in the present study, meaning that the tensile properties of the nonwoven geotextile were scaled down by a factor of 225 in the reduced model tests. A nonwoven geotextile with a low tensile strength and stiffness was employed to fulfill the similitude laws, which fall in the range of commercially available reinforcement materials.

Table 3. Scaling factors and corresponding values determined by scaling law

Parameters	Scaling factor[a]	Model	Prototype
Geometry			
GRS embankment height, H_E (m)	$1/N$	0.12	1.8
Foundation height, H_F (m)	$1/N$	0.2	3.0
Reinforcement parameter			
Ultimate tensile strength, T_{ult} (kN/m)	$1/N^2$	0.70	157.5
Stiffness, J_{50} (kN/m)	$1/N^2$	5.47	1,231
Soil parameter			
Target dry unit weight, γ_d (kN/m^3)	1	15.3	15.3
Friction angle, ϕ' (degrees)	1	39	39
Interface parameter			
Soil-geosynthetic friction angle, δ' (degrees)	1	27.4	27.4

[a]Target scaling factor $N = 15$.

J. Geotech. Geoenviron. Eng., 2025, 151(4): 04025018

Digital Image Analyses

In the unreinforced and reinforced foundation tests, the surface displacement profiles and shear strain contours induced by various magnitudes of reverse fault displacement were obtained using DIA techniques. Digital terrain models (DTMs) were established using images captured from the tops of the foundations during testing through the image analysis software PhotoScan (Agisoft LLC 2016) to determine the surface displacement profiles. Because deformation at the surface of a foundation induced by fault displacement critically influences the stability of a corresponding superstructure, β_{max}, defined as the maximum angular distortion at the ground surface, was employed in this study as a primary parameter to evaluate the performance of unreinforced and reinforced foundations. The angular distortion at the ground surface was derived from the surface displacement profile through the following formula:

$$\beta = \frac{d\delta}{dx} \tag{1}$$

where $d\delta$ and dx = vertical displacement and horizontal distance at two close points, respectively. β_{max} was then determined as the maximum value of β (i.e., the steepest slope) along the surface displacement profile. Furthermore, to evaluate the effectiveness of the GRS, GEC, and geocell foundations in reducing β_{max}, a percentage reduction in β_{max} was adopted in this study; this reduction was calculated as follows:

$$R_d = \frac{\beta_{max,u} - \beta_{max,r}}{\beta_{max,u}} \tag{2}$$

where $\beta_{max,u}$ and $\beta_{max,r}$ = maximum angular distortions of the unreinforced and reinforced foundations, respectively. The fault influence length, L_I, defined as the horizontal distance between two points across the fault outcrop that have $\beta = 0$ of the surface displacement, was also evaluated.

The shear strain contours were determined to explore the propagation of fault-induced shear rupture, and were obtained by analyzing the photographs captured from the front side of the foundations using a digital image correlation (DIC) software, Ncorr (Blaber et al. 2015). Black sand was uniformly mixed into the foundation soil and the movement of the soil particles was tracked by comparing the gray level of the images captured for the initial and deformed states. The shear strain contours were then determined using the established displacement field of each foundation. Notably, the shear strain contours were determined from the Lagrangian perspective to avoid noisy strain data. The shear strain developed in the foundations at a specific fault displacement was calculated based on the initial condition (i.e., before the occurrence of fault displacement). Details regarding the DIA technique for determination of surface displacement profiles, maximum angular distortion, and shear strain contours are discussed in the authors' contributed papers (Chiang et al. 2023; Yang et al. 2020).

In the reduced model tests conducted on the reinforced embankment and foundation systems, the horizontal displacement of the facing of the GRS embankment was measured using a Leica Geosystems laser distance meter (accuracy: ±1 mm). Measuring points were marked on the facing of the GRS embankment in matrix form, and the horizontal displacement at various fault displacements was determined. The maximum horizontal displacement of the facing (Δ_{max}) was then determined to evaluate the performance of the overlying GRS embankment when subjected to reverse fault movement.

Table 4. Experimental results of reinforced foundations at maximum fault displacement

Test ID	Maximum angular distortion β_{max}	Percentage reduction[a] R_d (%)	Influence length L_I (cm)
UF	1.07	—	28.2
GRF	1.07	0	34.1
GECF	0.78	27.1	40.5
GCF	0.62	42.1	31.8

[a]Compared to test UF.

Results of Reinforced Foundation Tests

This section presents the results of the unreinforced, GRS, GEC, and geocell foundation tests. The effectiveness and reinforcing mechanisms of the reinforced foundations for reducing the maximum angular distortion at the ground surface are discussed and compared. Table 4 summarizes the results of the unreinforced and reinforced foundation tests at maximum fault displacement (i.e., $S = 7.5$ cm). The test ID of the unreinforced and reinforced foundations shown in Table 4 are used hereinafter to simplify the discussion.

Results and Comparison of Shear Ruptures

Fig. 7 presents a series of images and shear strain contours for Test UF at various fault displacements. As the reverse fault displacement increased, the ground surface deformation became more evident (Fig. 8). The fault-induced shear rupture developed from the fault tip, and decreased in dip as it propagated toward the ground surface. The fault influence length was $L_I = 28.2$ cm at $S = 7.5$ cm. Notably, the width of the shear band, and hence the fault influence length, was affected by the particle size of the soil material (Garcia and Bray 2019; Anastasopoulos et al. 2007; Stone and Muir Wood 1992). The L_I values were employed to analyze the reinforcing mechanisms of reinforced foundations under reverse faulting. Moreover, the surface displacement profiles and shear strain contours indicate that there was no displacement at the left and right boundaries, and the fault-induced shear rupture did not extend to these boundaries. This observation suggests that the boundary conditions had a limited impact on ground surface deformation and the development of shear rupture.

Figs. 9–11 present a series of images and shear strain contours at various fault displacements for Test GRF, GECF, and GCF, respectively. Different reinforcing mechanisms and the development of fault-induced shear ruptures were observed for the different types of reinforced foundations. For the GRS foundation involving small fault displacements (i.e., $S/H_F < 15\%$), the fault-induced shear rupture was intercepted by the planar reinforcement [Fig. 9(b)]. However, the GRS foundation became ineffective at large fault displacements because the planar reinforcement can sustain only tension and not compression, and lost its reinforcing function when the GRS foundation was primarily subjected to compression at large fault movement (i.e., the hanging wall moved toward the footwall). The fault-induced shear rupture passed through the planar reinforcement and reached the ground at $S = 7.5$ cm ($S/H_F = 37.5\%$), as shown in Fig. 9(c).

For the GEC foundation, the fault-induced shear rupture was first diffused and then diverted by the GECs, resulting in a secondary shear rupture [Figs. 10(b and c)] and a stepped surface displacement profile (Fig. 8). The diffusion of the shear rupture was caused by the bending of the GECs, leading to the fault-induced shear rupture being distributed over a relatively wide influential fault zone. The fault influence length was $L_I = 40.5$ cm at

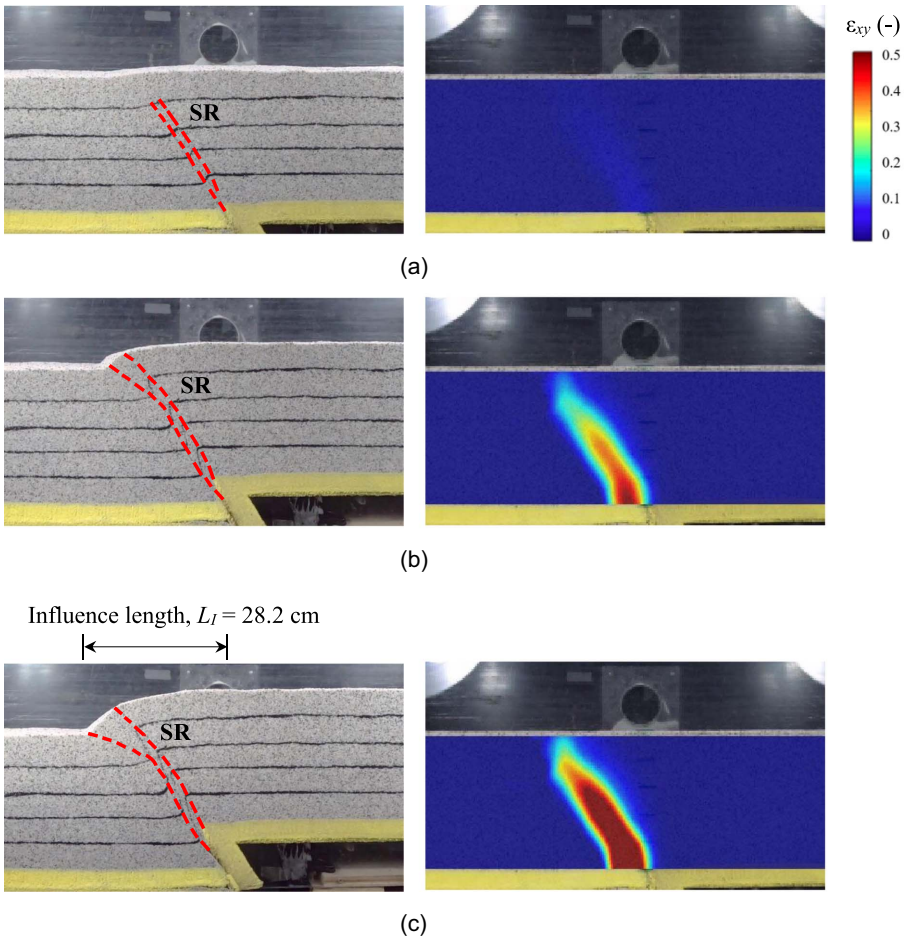

Fig. 7. Images and shear strain contours of test UF (unreinforced foundation) at S = (a) 1.5 cm; (b) 4.5 cm; and (c) 7.5 cm.

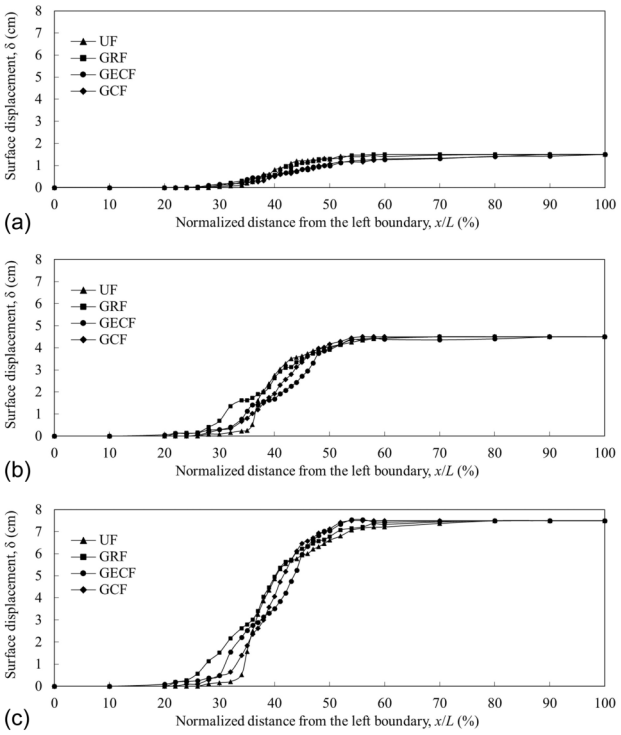

Fig. 8. Ground surface displacement profiles of foundations at S = (a) 1.5 cm; (b) 4.5 cm; and (c) 7.5 cm.

$S = 7.5$ cm, which was considerably longer than that observed in the unreinforced foundation (i.e., $L_I = 28.2$ cm). As the reverse fault further displaced, the lateral earth pressure (confining pressure) acting on the GECs increased, resulting in an increase in GEC stiffness. The GECs with high stiffness diverted the fault-induced shear rupture backward away from the GECs at large fault displacement [Fig. 10(c)], which further dissipated the energy of the fault movement.

For the geocell foundation, the fault-induced shear rupture was intercepted by the geocell mattress [Figs. 11(b and c)]. The confining stress provided by the geocell reinforcement increased the shear strength of the soil material inside the geocell and therefore intercepted the shear rupture. Furthermore, compared with a planar geotextile, the three-dimensional geocell mattress can provide bending stiffness against compressive forces induced by bending deformation and thus was able to disperse the imposed stress over a wider influential fault zone. Stress dispersion prevents the breakthrough of the shear rupture through the ground surface. Shear stress concentration was not observed at the ground surface, resulting in smooth surface displacement profiles (Fig. 8).

Results and Comparison of Ground Surface Deformation

Fig. 12 presents a comparison of β_{max} values at various fault displacements for the unreinforced and reinforced (GRS, GEC, and geocell) foundations. In test UF, the β_{max} value significantly increased from 0.25 to 0.75 as the fault-induced shear rupture

J. Geotech. Geoenviron. Eng., 2025, 151(4): 04025018

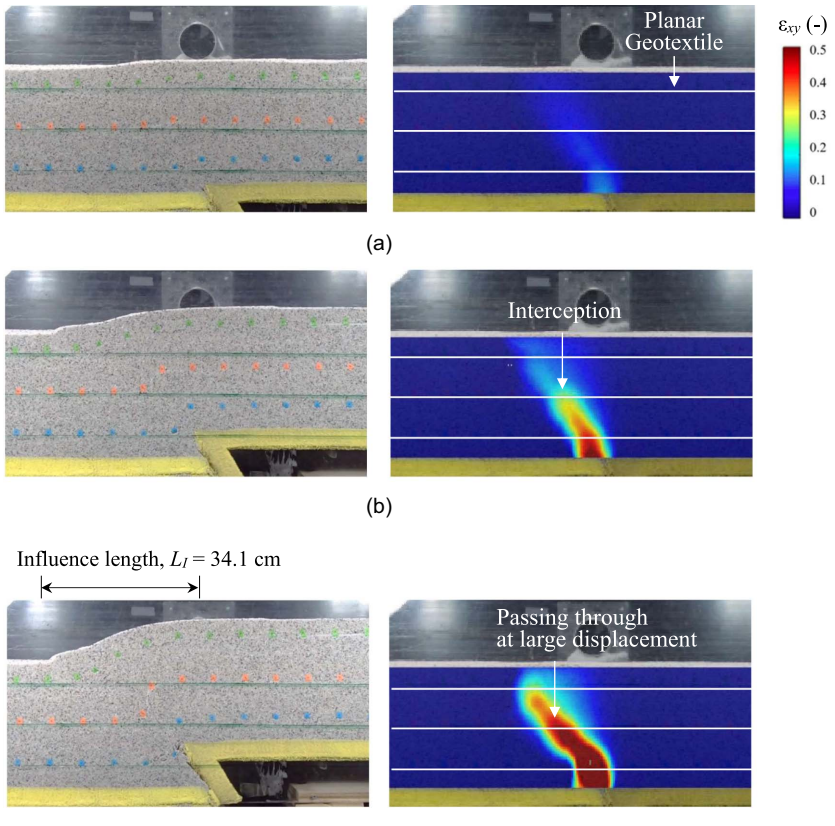

Fig. 9. Images and shear strain contours of test GRF (GRS foundation) at S = (a) 1.5 cm; (b) 4.5 cm; and (c) 7.5 cm.

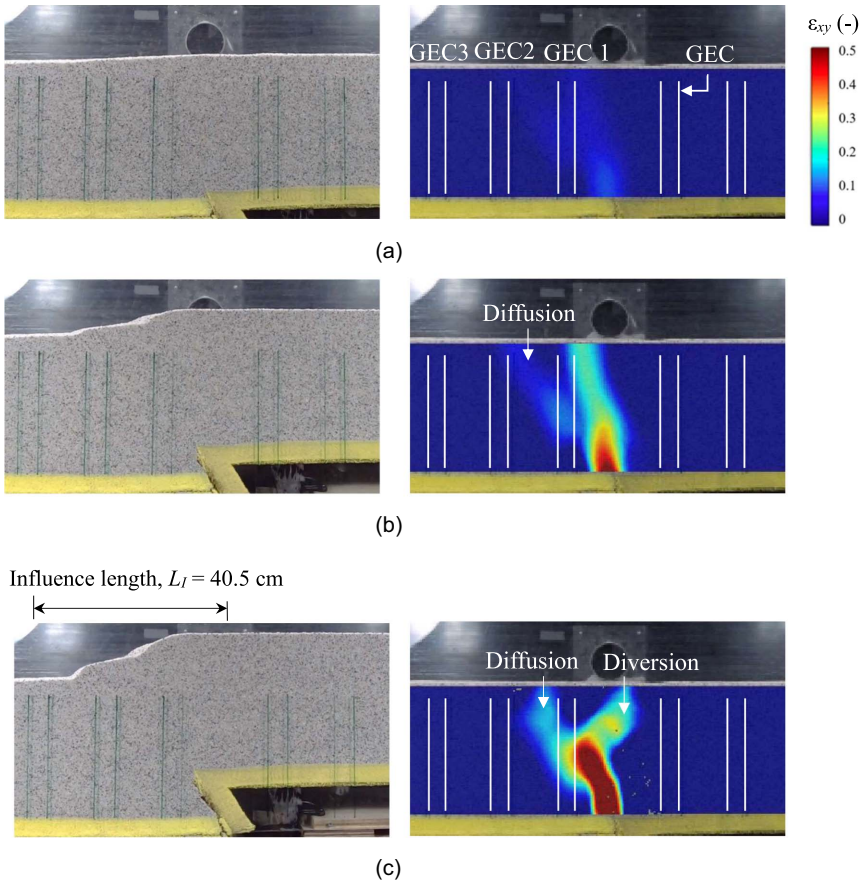

Fig. 10. Images and shear strain contours of test GECF (GEC foundation) at S = (a) 1.5 cm; (b) 4.5 cm; and (c) 7.5 cm.

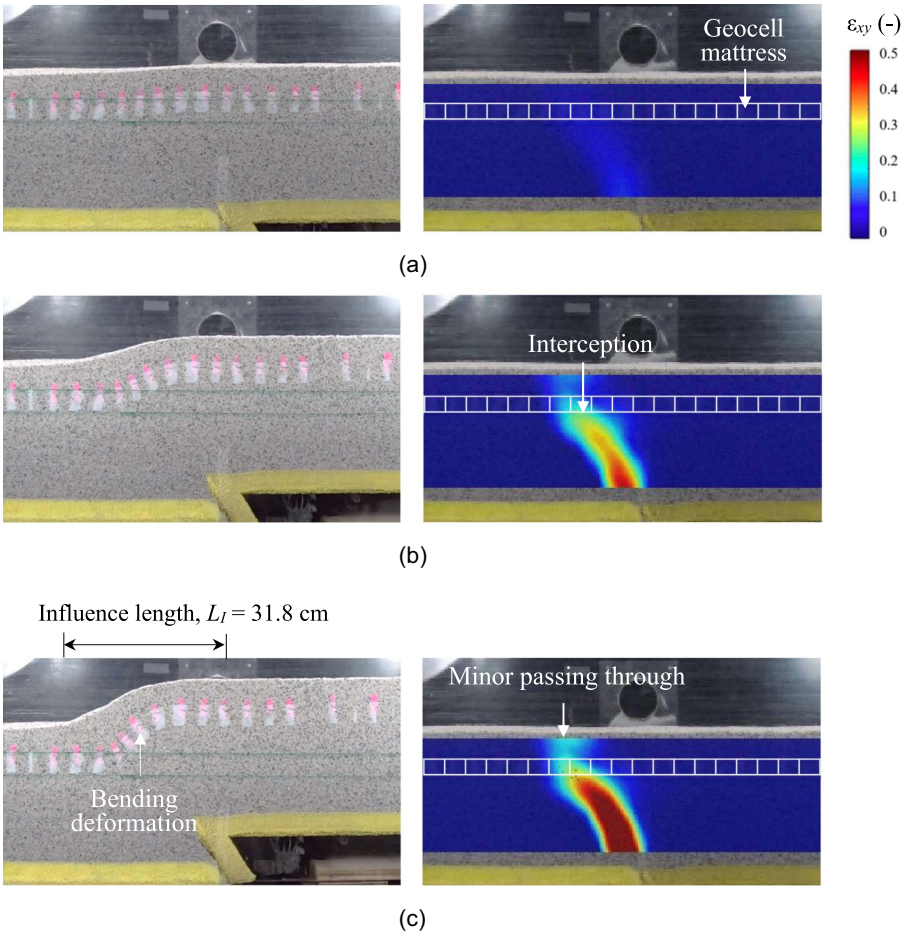

Fig. 11. Images and shear strain contours of test GCF (geocell foundation) at S = (a) 1.5 cm; (b) 4.5 cm; and (c) 7.5 cm.

approached the ground surface at $S = 3$ cm ($S/H_F = 15\%$). This value (i.e., $\beta_{max} = 0.75$) exceeds the angular distortion limits of no evident damage observed for wrapped-around GRS structures subjected to differential settlement (Miao et al. 2014; Viswanadham and Konig 2009), implying a high risk of surface fault hazard. However, with the inclusion of different types of reinforcement, the β_{max} at the ground surface considerably reduced to some extent.

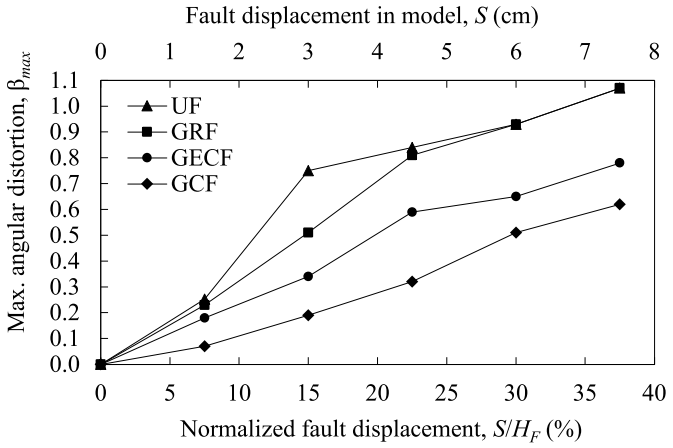

Fig. 12. Maximum angular distortion at the ground surface of different types of foundations.

Among all the reinforced foundations, the geocell foundation proved to be the most effective in reducing fault-induced angular distortion at the ground surface. The corresponding R_d value at the maximum fault displacement of $S = 7.5$ cm ($S/H_F = 37.5\%$) was 42.1%, which was higher than those of the GRS and GEC foundations, as summarized in Table 4. The GEC foundation had the second-best performance in reducing β_{max}, which had an R_d value of 27.1% at $S = 7.5$ cm ($S/H_F = 37.5\%$). The GRS foundation was able to reduce β_{max} only at small fault displacements ($S/H_F <$ 15%). However, the R_d value decreased to 0% when the fault displacement reached $S = 7.5$ cm ($S/H_F = 37.5\%$), meaning that the reinforcement was ineffective at larger fault displacements.

Results of Reinforced System Tests

This section presents the results of the reduced model tests conducted on the reinforced embankment and foundation systems, comprising a GRS embankment overlying an unreinforced foundation or a reinforced (GRS, GEC, or geocell) foundation. The maximum horizontal displacement measured on the wrapped-around facing of the GRS embankment (Δ_{max}), as well as the shear ruptures developed within the underlying unreinforced and reinforced foundations were compared and discussed. Table 5 summarizes the results corresponding to the GRS embankment and foundation systems at maximum fault displacement (i.e., $S = 7.5$ cm). For simplicity, the test ID of the reinforced embankment and foundation systems shown in Table 5 are used hereinafter. In other words,

J. Geotech. Geoenviron. Eng., 2025, 151(4): 04025018

Table 5. Experimental results of reinforced systems at maximum fault displacement

Test ID	Normalized maxi. facing displacement Δ_{max}/H_E (%)	Percentage reduction[a] R_d (%)
GRE + UF	19.17	—
GRE + GRF	17.50	8.7
GRE + GECF	12.50	34.8
GRE + GCF	11.67	39.1

[a]Compared to test GRE + UF.

the GRS embankment with unreinforced, GRS, GEC, and geocell foundations is referred to as test GRE + UF, test GRE + GRF, test GRE + GECF, and test GRE + GCF, respectively.

Results and Comparison of Shear Ruptures

Figs. 13–16 present the propagation of fault-induced shear ruptures at various fault displacements for tests GRE + UF, GRE + GRF, GRE + GECF, and GRE + GCF, respectively. The test results indicated that the development of shear ruptures was affected by the overburden pressure applied by the overlying GRS embankment. In test GRE + UF, in contrast to the development of a single shear rupture in test UF, two shear ruptures were observed in the unreinforced foundation with the GRS embankment (Figs. 7 and 13). The development of the primary shear rupture (labeled SR1 in Fig. 13) in the unreinforced foundation was constrained by the overburden pressure, and a secondary shear rupture (labeled SR2 in Fig. 13) was developed to dissipate the energy of the fault movement at larger fault displacements. For test GRE + GRF, compared with test GRF, a more pronounced interception of the shear rupture was observed in the GRS foundation with the GRS embankment (Figs. 9 and 14). The overburden pressure acting on the GRS foundation enhanced the soil–geosynthetics interaction and subsequently enhanced the shear rupture interception ability of the planar reinforcement.

For test GRE + GECF, similar to test GECF, the shear rupture was first diffused and then diverted by the GECs (Figs. 10 and 15). However, less diffusion [Fig. 15(b)] and more significant diversion [Fig. 15(c)] of shear ruptures were observed in test GRE + GECF than in test GECF at the same magnitude of fault displacement. The overburden pressure applied by the GRS embankment increased the degree of confinement acting on the GECs and thus also increased the GEC stiffness, resulting in considerable diversion of the shear rupture. Finally, the shear rupture interception was more significant in test GRE + GCF than in test GCF (Figs. 11 and 16). An intense concentration of shear strain was observed in the soil layer between the geocell mattress and the GRS embankment owing to the effect of overburden pressure, which restrained soil deformation and thus increased the soil shear strain.

Results and Comparison of Wall Facing Deformation

The facing deformation was attributed to two factors: (1) an increase in lateral earth pressure acting on the facing because of compression; and (2) the presence of different settlements induced by the reverse fault movement, resulting in the deformation of the GRS embankment facing. Fig. 17 shows the normalized maximum

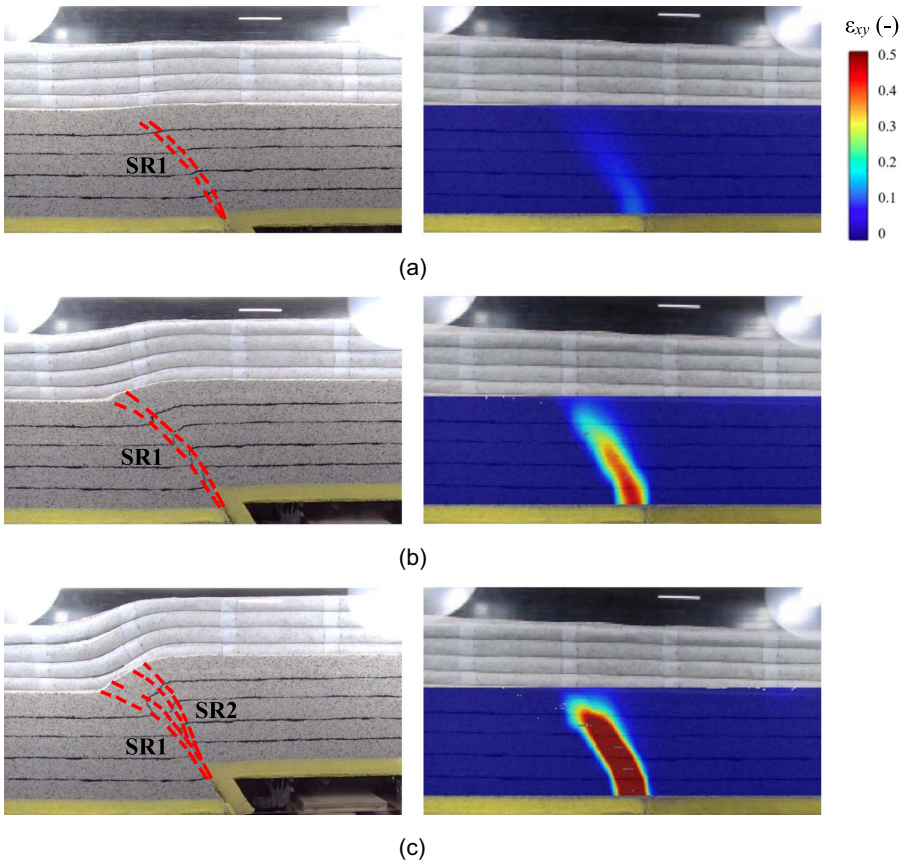

Fig. 13. Images and shear strain contours of test GRE + UF at S = (a) 1.5 cm; (b) 4.5 cm; and (c) 7.5 cm.

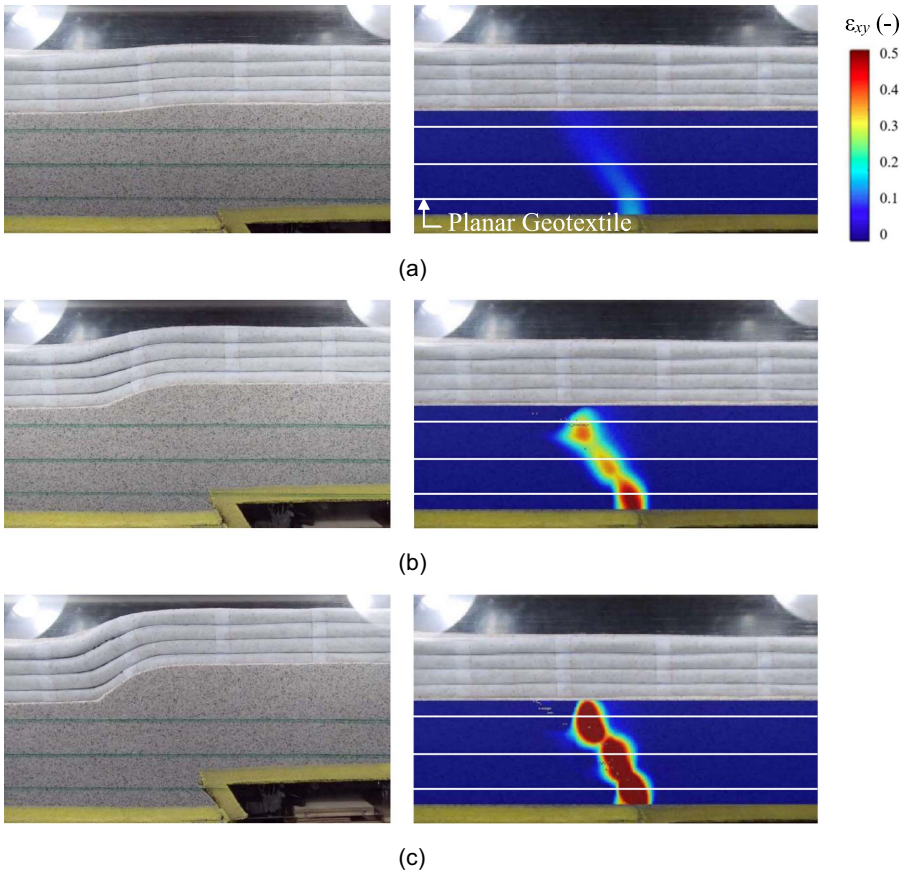

Fig. 14. Images and shear strain contours of test GRE + GRF at S = (a) 1.5 cm; (b) 4.5 cm; and (c) 7.5 cm.

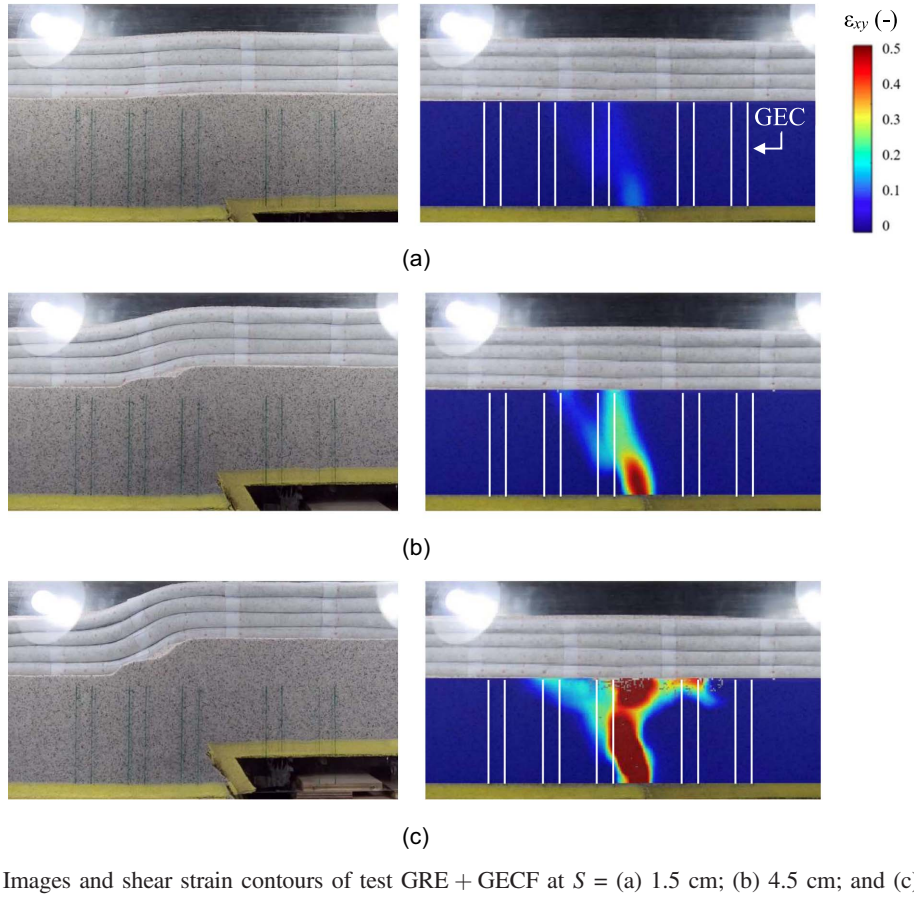

Fig. 15. Images and shear strain contours of test GRE + GECF at S = (a) 1.5 cm; (b) 4.5 cm; and (c) 7.5 cm.

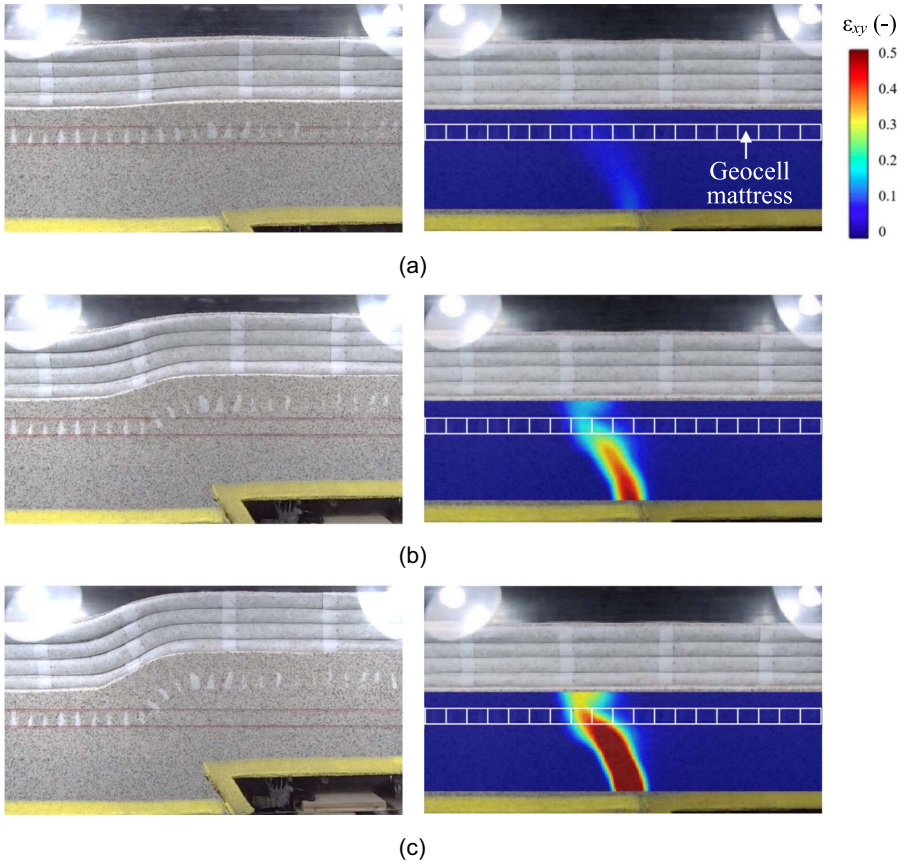

Fig. 16. Images and shear strain contours of test GRE + GCF at S = (a) 1.5 cm; (b) 4.5 cm; and (c) 7.5 cm.

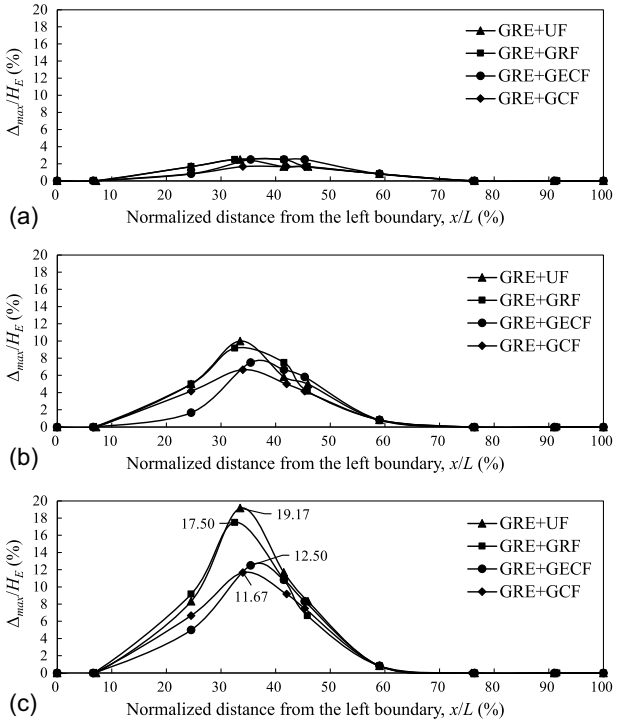

Fig. 17. Normalized maximum facing displacement measured in the longitudinal direction of the GRS embankment at S = (a) 1.5 cm; (b) 4.5 cm; and (c) 7.5 cm.

horizontal displacement (i.e., $\Delta_{\max}/H_E$) measured in the longitudinal direction of the wrapped-around facing of the GRS embankment at various fault displacements. The test results revealed that for all the GRS embankment and foundation systems, the overlying GRS embankment remained stable, and only localized deformation on the wrapped-around facing was observed as the fault displacement was applied up to $S = 7.5$ cm. The localized deformation of the facing corresponded to the location of the shear rupture outcrop, where the facing experienced maximum shear stress.

Fig. 18 presents comparisons of maximum facing displacement profiles for all the reinforced embankment and foundation systems at various fault displacements. These profiles were determined at the cross-section where the facing exhibited maximum horizontal displacement and was normalized by the height of the GRS embankment. Fig. 18 indicates that the facing of the GRS embankment gradually deformed with the fault displacement. Because the folded back length of the top reinforcement layer (Fig. 4) and the overburden pressure acting on the bottom reinforcement layers were sufficient, the $\Delta_{\max}$ occurred at the second reinforcement layer of the GRS embankment owing to relatively low pullout resistance, which was located at two-thirds of the facing height (i.e., $2/3H_E$) from the bottom of the GRS embankment.

Fig. 18 also indicates that the geocell foundation had the most optimal effects in minimizing the maximum facing displacement of the GRS embankment, especially at larger fault displacements. The normalized maximum facing displacements for tests GRE + UF, GRE + GRF, GRE + GECF, and GRE + GCF at $S = 7.5$ cm were $\Delta_{\max}/H_E = 19.17\%$, 17.5%, 12.5%, and 11.67%, respectively.

J. Geotech. Geoenviron. Eng., 2025, 151(4): 04025018

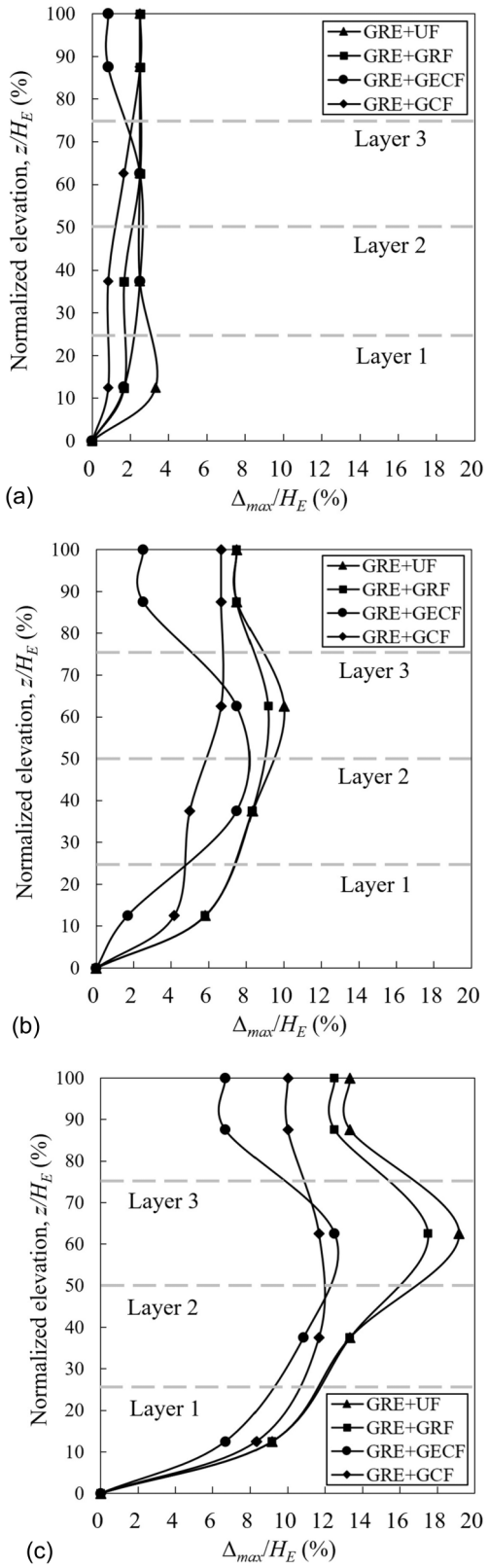

Fig. 18. Normalized maximum facing displacement profiles for each reinforced system at S = (a) 1.5 cm; (b) 4.5 cm; and (c) 7.5 cm.

The order of the magnitude of Δ_{max} was GRE + UF > GRE + GRF > GRE + GECF > GRE + GCF, corresponding to the magnitude of β_{max} induced by reverse fault movement (see Fig. 12). Compared with test GRE + UF, test GRE + GCF (when a geocell was involved) had a 39.1% reduction in the Δ_{max} value at $S = 7.5$ cm. The GEC foundation (test GRE + GECF) exhibited the second-best performance in reducing the maximum facing displacement of the GRS embankment, achieving a reduction of 34.8% in the Δ_{max} value at $S = 7.5$ cm. Notably, although the test GRF (i.e., GRS foundation) results indicated that the GRS foundation lost its effectiveness at large fault displacements (i.e., $R_d = 0\%$ at $S \geq 6$ cm), the Δ_{max} determined in test GRE + GRF was observed to be lower than that of test GRE + UF. This finding suggests that the GRS foundation can still provide a reinforcing function to a certain extent at large fault displacement when placed under the GRS embankment.

Design Implications

Fig. 19 illustrates the variations in normalized maximum facing displacement with fault displacements for all reinforced embankment and foundation systems. The Δ_{max}/H_E ranges for serviceability ($\Delta_{max}/H_E = 1.5\%$–3.5%) and limit states ($\Delta_{max}/H_E = 8\%$–12%) of GRS walls are presented as green and red zones in Fig. 19, respectively. The Δ_{max}/H_E range for the serviceability state of GRS walls was determined based on design guidelines for GRS walls (AASHTO 2012; NCMA 2010; Berg et al. 2009; WSDOT 2005; Elias et al. 2001), which suggest that GRS walls can remain stable as the maximum facing displacement remains between 1.5% and 3.5% of the wall height ($\Delta_{max}/H_E = 1.5\%$–3.5%). Additionally, the Δ_{max}/H_E range for the limit state of GRS walls was determined based on centrifuge tests conducted by Hung et al. (2020), which indicated that GRS walls reach the limit state as the normalized maximum facing displacement was $\Delta_{max}/H_E = 8\%$–12%. Furthermore, the corresponding Richter magnitudes (M_L) and earthquake classifications (i.e., strong, moderate, and light earthquakes) for different fault displacements are also presented in Fig. 19. The conversion between fault displacement and earthquake magnitude, as well as the earthquake classifications, were discussed in Chiang et al. (2023).

Fig. 19 revealed that when a moderate earthquake ($5.0 \leq M_L < 6.0$) occurs, all reinforced embankment and foundation systems (i.e., GRS embankments with unreinforced, GRS, GEC, and geocell foundations) can maintain their stability and serviceability as the Δ_{max}/H_E induced by the fault movement remains in the green zone. However, as a strong earthquake ($M_L \geq 6.0$) occurs, the GRS embankment with unreinforced, GRS, or GEC foundations exceeds the limit state because of the excessive horizontal facing displacement, indicating that the GRS embankment may collapse because of the influence of fault displacement at this level. This finding was also proven by the reduced model tests conducted on the reinforced systems, which revealed that at large fault displacement, substantial facing displacement occurred at the second reinforcement layer in tests GRE + UF, GRE + GRF, and GRE + GECF [see Fig. 18(c)], whereas gradual facing displacement was observed in test GRE + GCF. Notably, the GRS embankments with underlaid geocell foundations remained within the Δ_{max}/H_E range for the limit state when a strong earthquake was simulated, suggesting that the GRS embankment may experience large deformation but collapse may not occur. Local deformation can easily be repaired after an earthquake to restore the design function of a highway embankment. In summary, when a highway is required to cross an active fault, a reinforced embankment and foundation system consisting of a wrapped-around GRS embankment overlying a geocell foundation is recommended to mitigate the surface fault hazards associated with reverse fault movement.

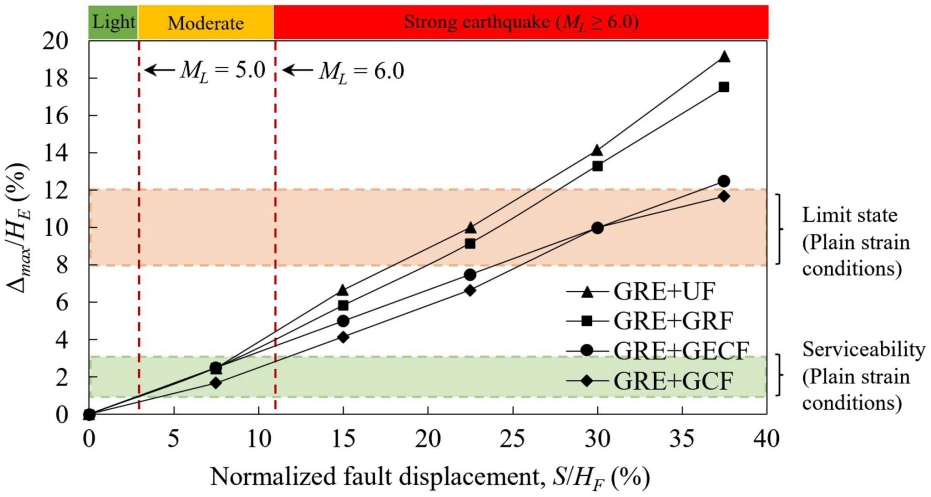

Fig. 19. Overall evaluation of geosynthetic-reinforced embankment and foundation systems against reverse fault movement.

Conclusions

This paper presents a series of reduced model tests on three types of reinforced foundations, including GRS, GEC, and geocell foundations. For comparison, a reduced model test was also performed on an unreinforced foundation. The effectiveness and reinforcing mechanisms of the GRS, GEC, and geocell foundations in reducing the maximum angular distortion induced by reverse fault displacement were investigated. Furthermore, another series of reduced model tests were conducted on the reinforced embankment and foundation systems comprising a GRS embankment overlying the unreinforced and reinforced foundations to analyze the overall performance of the reinforced systems against reverse fault movement. On the basis of the results of the reduced model tests, the following conclusions of the present study are presented:

- The geocell foundation proved to be the most effective in reducing β_{max} at the ground surface. The corresponding R_d value at $S/H_F = 37.5\%$ was 42.1%. The GEC foundation had the second-best performance in reducing the β_{max} value, which had an R_d value of 27.1% at $S/H_F = 37.5\%$. The GRS foundation was only able to minimize the β_{max} value at small fault displacements ($S/H_F < 15\%$). The R_d value decreased to 0% at $S/H_F = 37.5\%$.
- Different reinforcing mechanisms for the reinforced foundations subject to reverse fault movement were identified. The fault-induced shear rupture was intercepted by the GRS foundation at small fault displacement, while diffusion and diversion effects were observed for GEC foundations. For the geocell foundation, the bending stiffness of the geocell mattress dispersed the imposed stress over a wider influential area and prevented the breakthrough of the shear rupture through the ground surface.
- For all the reinforced embankment and foundation systems, the overlying GRS embankment remained stable. Only localized deformation on the wrapped-around facing was observed at where the facing experienced the maximum shear stress. The Δ_{max} occurred at two-thirds of the facing height (i.e., $2/3H_E$) from the bottom of the GRS embankment because of the insufficient pullout resistance of the reinforcement, resulting in large deformation.
- The geocell foundation had the most optimal effects in minimizing the Δ_{max} of the GRS embankment. Compared with test GRE+UF, the Δ_{max} at $S/H_F = 37.5\%$ was reduced by 39.1% when a geocell foundation was involved. The GEC foundation exhibited the second-best performance in reducing Δ_{max}, which had a reduction of 34.8% at $S/H_F = 37.5\%$.
- All of the reinforced embankment and foundation systems evaluated in the present study can remain serviceable when a moderate earthquake occurs ($5.0 \leq M_L < 6.0$). When a strong earthquake occurs ($M_L \geq 6.0$), the GRS embankment with unreinforced, GRS, and GEC foundations exceeds the limit state; only the GRS embankment with an underlaid geocell foundation remains within the limit state in such a case, indicating that even if the GRS embankment experiences large deformation, collapse may not occur.
- This study aimed to understand the overall effectiveness and reinforcing mechanisms of reinforced systems in mitigating ground surface deformation associated with reverse fault movement. The influences of material properties, design parameters (e.g., dimensions and reinforcement layout of reinforced systems), and stress levels on the performance of reinforced systems in response to reverse fault movement need to be further studied by numerical simulations and centrifuge modelings.

Data Availability Statement

Some or all data, models, or code that support the findings of this study are available from the corresponding author upon reasonable request.

Acknowledgments

This research was inspired by a real construction project featuring a GRS structure across an active fault in Central Taiwan, designed by Sinotech Engineering Consultants. The authors extend sincere gratitude to Sinotech for providing the design and construction details. This research was supported by the National Science and Technology Council of Taiwan under Grants Nos. MOST110-2628-E-002-003 and NSTC 112-2811-E-002-001.

References

AASHTO. 2012. *AASHTO LRFD bridge design specifications*. 6th ed. Washington, DC: AASHTO.

Abid, M. S., D. Rathod, and S. K. Vanapalli. 2022. "Bearing capacity of annulus stone column double-encapsulated with geotextiles." *Int. J. Geomech.* 23 (2): 04022281. https://doi.org/10.1061/IJGNAI.GMENG-7817.

Agisoft LLC. 2016. *Agisoft PhotoScan user manual professional edition, version 1.2*. St. Petersburg, Russia: Agisoft LLC.

Ahmadi, N., and M. Fadaee. 2023. "Mechanical behavior of soil foundations reinforced with geosynthetics exposed to normal and reverse fault ruptures." *Period. Polytech., Civ. Eng.* 67 (1): 123–140. https://doi.org/10.3311/PPci.20491.

Al Heib, M., M. Hassoun, F. Emeriault, P. Villard, and A. Farhat. 2021. "Predicting subsidence of cohesive and granular soil layers reinforced by geosynthetic." *Environ. Earth Sci.* 80 (70): 1–24. https://doi.org/10.1007/s12665-020-09350-3.

Almeida, M. S. S., I. Hosseinpour, M. Riccio, and D. Alexiew. 2014. "Behavior of geotextile encased granular columns supporting test embankment on soft deposit." *J. Geotech. Geoenviron. Eng.* 141 (3): 04014116. https://doi.org/10.1061/(ASCE)GT.1943-5606.0001256.

Anastasopoulos, I., G. Gazetas, M. F. Bransby, M. C. R. Davies, and A. El Nahas. 2007. "Fault rupture propagation through sand: Finite element analysis and validation through centrifuge experiments." *J. Geotech. Geoenviron. Eng.* 133 (8): 943–958. https://doi.org/10.1061/(ASCE)1090-0241(2007)133:8(943).

Ardah, A., M. Y. Abu-Farsakh, and G. Z. Voyiadjis. 2018. "Numerical evaluation of the effect of differential settlement on the performance of GRS-IBS." *Geosynth. Int.* 25 (4): 427–441. https://doi.org/10.1680/jgein.18.00026.

Ari, A., and G. Misir. 2021. "Three-dimensional numerical analysis of geocell reinforced shell foundations." *Geotext. Geomembr.* 49 (4): 963–975. https://doi.org/10.1016/j.geotexmem.2021.01.006.

Ashtiani, M., A. Ghalandarzadeh, M. Mahdavi, and M. Hedayati. 2018. "Centrifuge modeling of geotechnical mitigation measures for shallow foundations subjected to reverse faulting." *Can. Geotech. J.* 55 (8): 1130–1143. https://doi.org/10.1139/cgj-2017-0093.

ASTM. 2011. *Standard test method for tensile properties of geotextiles by the wide-width strip method*. ASTM D4595. West Conshohocken, PA: ASTM.

ASTM. 2015. *Standard test method for consolidated drained triaxial compression test for soils*. ASTM D7181. West Conshohocken, PA: ASTM.

Berg, R., B. R. Christopher, and N. Samtani. 2009. *Design and construction of mechanically stabilized earth walls and reinforced soil slopes*. Washington, DC: Federal Highway Administration.

Biabani, M. M., N. T. Ngo, and B. Indraratna. 2016. "Performance evaluation of railway subballast stabilised with geocell based on pull-out testing." *Geotext. Geomembr.* 44 (4): 579–591. https://doi.org/10.1016/j.geotexmem.2016.03.006.

Blaber, J., B. Adair, and A. Antoniou. 2015. "Ncorr: Open-source 2D digital image correlation Matlab software." *Exp. Mech.* 55 (6): 1105–1122. https://doi.org/10.1007/s11340-015-0009-1.

Bonilla, M. G. 1967. *Historic surface faulting in the continental United States and adjacent parts of Mexico.* Washington, DC: USGS.

Bray, J. D. 2001. "Developing mitigation measures for the hazards associated with earthquake surface fault rupture." In *A workshop on seismic fault-induced failures—Possible remedies for damage to urban facilities*. Tokyo: Univ. of Tokyo.

Bray, J. D. 2009. "Earthquake surface fault rupture design considerations." In *Proc., Sixth Int. Conf. on Urban Earthquake Engineering*, 37–45. Tokyo: Center for Urban Earthquake Engineering, Tokyo Institute of Technology.

Bray, J. D., A. Ashmawy, G. Mukhopadhyay, and E. M. Gath. 1993. "Use of geosynthetics to mitigate earthquake fault rupture propagation through compacted fill." In Vol. 1 of *Proc., Geosynthetics'93 Conf.*, 379–392. St. Paul, MN: Industrial Fabrics Association International.

Bray, J. D., and F. E. Garcia. 2022. "Discrete element analysis of earthquake surface fault rupture through layered media." *Soil Dyn. Earthquake Eng.* 152 (Jan): 107021. https://doi.org/10.1016/j.soildyn.2021.107021.

Buckingham, E. 1914. "On physically similar systems; illustrations of the use of dimensional equations." *Phys. Rev.* 4 (4): 345–376. https://doi.org/10.1103/PhysRev.4.345.

Cengiz, C., I. E. Kilic, and E. Guler. 2019. "On the shear failure mode of granular column embedded unit cells subjected to static and cyclic shear loads." *Geotext. Geomembr.* 47 (2): 193–202. https://doi.org/10.1016/j.geotexmem.2018.12.011.

Changizi, F., A. Razmkhah, H. Ghasemzadeh, and M. Amelsakhi. 2021. "Behavior of geocell reinforced soil abutment wall: A physical modeling." *J. Mater. Civ. Eng.* 34 (3): 04021495. https://doi.org/10.1061/(ASCE)MT.1943-5533.0004132.

Chen, J. F., L. Y. Li, J. F. Xue, and S. Z. Feng. 2015. "Failure mechanism of geosynthetic encased stone columns in soft soils under embankment." *Geotext. Geomembr.* 43 (5): 424–431. https://doi.org/10.1016/j.geotexmem.2015.04.016.

Chen, J. F., X. T. Wang, J. F. Xue, Y. Zeng, and S. Z. Feng. 2018. "Uniaxial compression behavior of geotextile encased stone columns." *Geotext. Geomembr.* 46 (3): 277–283. https://doi.org/10.1016/j.geotexmem.2018.01.003.

Chen, Y.-G., W.-S. Chen, J.-C. Lee, Y.-H. Lee, and C.-T. Lee. 2001. "Surface rupture of 1999 Chi-Chi earthquake yields insights on active tectonics of central Taiwan." *Bull. Seismol. Soc. Am.* 91 (5): 977–985. https://doi.org/10.1785/0120000721.

Chiang, J., E. E. Michel, K.-H. Yang, and J. G. Zornberg. 2023. "Mitigation of reverse faulting in foundation soils using geosynthetic-encased granular columns." *Transp. Geotech.* 42 (Sep): 101067. https://doi.org/10.1016/j.trgeo.2023.101067.

Delli Carpini, M., P. Villard, and F. Emeriault. 2024. "Investigation of load transfer mechanisms in reinforced cohesive soil embankments in case of subsidence using DEM." *Geotext. Geomembr.* 52 (5): 912–924. https://doi.org/10.1016/j.geotexmem.2024.05.004.

Elias, V., B. R. Christopher, and R. Berg. 2001. *Mechanically stabilized earth walls and reinforced soil slopes design and construction guidelines*. Washington, DC: National Highway Institute, Federal Highway Administration.

Garcia, E. F., C. P. K. Gallage, and T. Uchimura. 2007. "Function of permeable geosynthetics in unsaturated embankments subjected to rainfall infiltration." *Geosynth. Int.* 14 (2): 89–99. https://doi.org/10.1680/gein.2007.14.2.89.

Garcia, F. E., and J. D. Bray. 2018. "Distinct element simulations of earthquake fault rupture through materials of varying density." *Soils Found.* 58 (4): 986–1000. https://doi.org/10.1016/j.sandf.2018.05.009.

Garcia, F. E., and J. D. Bray. 2019. "Discrete element analysis of earthquake fault rupture-soil-foundation interaction." *J. Geotech. Geoenviron. Eng.* 145 (9): 04019046. https://doi.org/10.1061/(ASCE)GT.1943-5606.0002092.

Gedela, R., S. Kalla, N. Sudarsanan, and R. Karpurapu. 2021. "Assessment of load distribution mechanism in geocell reinforced foundation beds using Digital Imaging Correlation Techniques." *Transp. Geotech.* 31 (Nov): 100664. https://doi.org/10.1016/j.trgeo.2021.100664.

Gu, M., J. Han, and M. Zhao. 2017. "Three-dimensional discrete-element method analysis of stresses and deformations of a single geogrid-encased stone column." *Int. J. Geomech.* 17 (9): 04017070. https://doi.org/10.1061/(ASCE)GM.1943-5622.0000952.

Gu, M., M. Zhao, L. Zhang, and J. Han. 2016. "Effects of geogrid encasement on lateral and vertical deformations of stone columns in model tests." *Geosynth. Int.* 23 (2): 100–112. https://doi.org/10.1680/jgein.15.00035.

Hajiazizi, M., A. Mazaheri, and R. P. Orense. 2018. "Analytical approach to evaluate stability of pile-stabilized slope." *Sci. Iran.* 25 (5): 2525–2536. https://doi.org/10.24200/sci.2017.4218.

Hajiazizi, M., E. Nemati, M. Nasiri, M. Bavali, and M. Sharifipur. 2020. "Optimal location of stone column for stabilization of sand slope: An experimental and 3D numerical investigation." *Sci. Iran.* 27 (1): 105–116. https://doi.org/10.24200/SCI.2018.20331.

Hasan, M., and N. K. Samadhiya. 2017. "Performance of geosynthetic-reinforced granular piles in soft clays: Model tests and numerical analysis." *Comput. Geotech.* 87 (Jul): 178–187. https://doi.org/10.1016/j.compgeo.2017.02.016.

Hegde, A., and T. G. Sitharam. 2015. "3-dimensional numerical modelling of geocell reinforced sand beds." *Geotext. Geomembr.* 43 (2): 171–181. https://doi.org/10.1016/j.geotexmem.2014.11.009.

Hong, Y.-S., C.-S. Wu, and Y.-S. Yu. 2016. "Model tests on geotextile-encased granular columns under 1-g and undrained conditions." *Geotext. Geomembr.* 44 (1): 13–27. https://doi.org/10.1016/j.geotexmem.2015.06.006.

Hosseinpour, I., M. S. S. Almeida, and M. Riccio. 2015. "Full-scale load test and finite-element analysis of soft ground improved by geotextile-encased granular columns." *Geosynth. Int.* 22 (6): 428–438. https://doi.org/10.1680/jgein.15.00023.

Hung, W. Y., K. H. Yang, T. S. Nguyen, and T. N. P. Pham. 2020. "Performance of geosynthetic-reinforced soil walls at failure." *J. GeoEng.* 15 (1): 13–29. https://doi.org/10.6310/jog.202003_15(1).2.

Khan, A., A. J. Puppala, and N. Biswas. 2023. "Evaluation of the structural performance of the geocell-stabilized flexible pavement." *Transp. Geotech.* 41 (Jul): 101021. https://doi.org/10.1016/j.trgeo.2023.101021.

Khorsandiardebili, N., and M. Ghazavi. 2021. "Static stability analysis of geocell-reinforced slopes." *Geotext. Geomembr.* 49 (3): 852–863. https://doi.org/10.1016/j.geotexmem.2020.12.012.

Lazarte, C. A., and J. D. Bray. 1996. "A study of strike-slip faulting using small-scale models." *Geotech. Test. J.* 19 (2): 118–129. https://doi.org/10.1520/GTJ10335J.

Lazarte, C. A., J. D. A. M. Bray, and R. E. Lemmer. 1994. "Surface breakage of the 1992 landers earthquake and its effects on structures." *Bull. Seismol. Soc. Am.* 84 (3): 547–561. https://doi.org/10.1785/BSSA0840030547.

Li, C.-H., M.-L. Lin, and W.-C. Huang. 2019. "Interaction between pile groups and thrust faults in a physical sandbox and numerical analysis." *Eng. Geol.* 252 (Mar): 65–77. https://doi.org/10.1016/j.enggeo.2019.02.023.

Liu, C.-N., K.-H. Yang, and M. D. Nguyen. 2014. "Behavior of geogrid-reinforced sand and effect of reinforcement anchorage under large-scale plane strain compression." *Geotext. Geomembr.* 42 (5): 479–493. https://doi.org/10.1016/j.geotexmem.2014.07.007.

Mehdipour, I., M. Ghazavi, and R. Z. Moayed. 2013. "Numerical study on stability analysis of geocell reinforced slopes by considering the bending effect." *Geotext. Geomembr.* 37 (Apr): 23–34. https://doi.org/10.1016/j.geotexmem.2013.01.001.

Miao, L., F. Wang, J. Han, and W. Lv. 2014. "Benefits of geosynthetic reinforcement in widening of embankments subjected to foundation differential settlement." *Geosynth. Int.* 21 (5): 321–332. https://doi.org/10.1680/gein.14.00019.

Mohapatra, S. R., K. Rajagopal, and J. Sharma. 2016. "Direct shear tests on geosynthetic-encased granular columns." *Geotext. Geomembr.* 44 (3): 396–405. https://doi.org/10.1016/j.geotexmem.2016.01.002.

Moosavi, S. M., and M. K. Jafari. 2012. "Investigation of the surface fault rupture hazard mitigation by geosynthetics." In *Proc., 15th World Conf. on Earthquake Engineering*. Lisbon, Portugal: Sociedade Portuguesa de Engenharia Sísmica.

NCMA (National Concrete Masonry Association). 2010. *Design manual for segmental retaining walls.* Edited by M. Bernardi. Herndon, VA: National Concrete Masonry Association.

Oettle, N. K., and J. D. Bray. 2013. "Geotechnical mitigation strategies for earthquake surface fault rupture." *J. Geotech. Geoenviron. Eng.* 139 (11): 1864–1874. https://doi.org/10.1061/(ASCE)GT.1943-5606.0000933.

Pokharel, S. K., J. Han, D. Leshchinsky, R. L. Parsons, and I. Halahmi. 2010. "Investigation of factors influencing behavior of single geocell-reinforced bases under static loading." *Geotext. Geomembr.* 28 (6): 570–578. https://doi.org/10.1016/j.geotexmem.2010.06.002.

Rahimi, M., S. N. Moghaddas Tafreshi, B. Leshchinsky, and A. R. Dawson. 2018. "Experimental and numerical investigation of the uplift capacity of plate anchors in geocell-reinforced sand." *Geotext. Geomembr.* 46 (6): 801–816. https://doi.org/10.1016/j.geotexmem.2018.07.010.

Rasouli, H., and B. Fatahi. 2021. "Geosynthetics reinforced interposed layer to protect structures on deep foundations against strike-slip fault rupture." *Geotext. Geomembr.* 49 (3): 722–736. https://doi.org/10.1016/j.geotexmem.2020.11.011.

Rathod, D., M. S. Abid, and S. K. Vanapalli. 2021. "Performance of polypropylene textile encased stone columns." *Geotext. Geomembr.* 49 (1): 222–242. https://doi.org/10.1016/j.geotexmem.2020.10.025.

Sitharam, T. G., and S. Sireesh. 2005. "Behavior of embedded footings supported on geogrid cell reinforced foundation beds." *Geotech. Test. J.* 28 (5): 452–463. https://doi.org/10.1520/GTJ12751.

Stone, K. J. L., and D. Muir Wood. 1992. "Effects of dilatancy and particle size observed in model tests on sand." *Soils Found.* 32 (4): 43–57. https://doi.org/10.3208/sandf1972.32.4_43.

Tafreshi, S. M., and A. R. Dawson. 2010. "Comparison of bearing capacity of a strip footing on sand with geocell and with planar forms of geotextile reinforcement." *Geotext. Geomembr.* 28 (1): 72–84. https://doi.org/10.1016/j.geotexmem.2009.09.003.

Tang, X., and M. Yang. 2013. "Investigation of flexural behavior of geocell reinforcement using three-layered beam model testing." *Geotech. Geol. Eng.* 31 (2): 753–765. https://doi.org/10.1007/s10706-013-9625-7.

Thallak, S. G., S. Saride, and S. K. Dash. 2007. "Performance of surface footing on geocell-reinforced soft clay beds." *Geotech. Geol. Eng.* 25 (May): 509–524. https://doi.org/10.1007/s10706-007-9125-8.

Viswanadham, B. V. S., and D. Konig. 2004. "Studies on scaling and instrumentation of a geogrid." *Geotext. Geomembr.* 22 (5): 307–328. https://doi.org/10.1016/S0266-1144(03)00045-1.

Viswanadham, B. V. S., and D. Konig. 2009. "Centrifuge modeling of geotextile-reinforced slopes subjected to differential settlements." *Geotext. Geomembr.* 27 (2): 77–88. https://doi.org/10.1016/j.geotexmem.2008.09.008.

WSDOT (Washington State DOT). 2005. "Abutments, retaining walls, and reinforced slopes." Chap. 15 in *Geotechnical design manual*. Olympia, Washington: WSDOT.

Yang, K.-H., J. Chiang, C.-W. Lai, J. Han, and M.-L. Lin. 2020. "Performance of geosynthetic-reinforced soil foundation across a normal fault." *Geotext. Geomembr.* 48 (3): 357–373. https://doi.org/10.1016/j.geotexmem.2019.12.007.

Yasuhara, K., and J. Recio-Molina. 2007. "Geosynthetic-wrap around revetments for shore protection." *Geotext. Geomembr.* 25 (4–5): 221–232. https://doi.org/10.1016/j.geotexmem.2007.02.004.

Yin, C., J. He, A. A. K. Gowi, Z. Li, and C. Zhou. 2024. "Effective stiffness matrix calculation of geocell layer and reinforcement mechanism analysis of geocell reinforced embankment." *Geotext. Geomembr.* 52 (4): 704–724. https://doi.org/10.1016/j.geotexmem.2024.03.010.

Yoo, C., J. W. Tabish, Q. Yang, J. S. Abbas, and S. Song. 2022. "Effect of internal drainage on deformation behavior of GRS wall during rainfall." *Geosynth. Int.* 29 (2): 137–150. https://doi.org/10.1680/jgein.21.00015.

Zhang, G., and L. Wang. 2017. "Simplified evaluation on the stability level of pile-reinforced slopes." *Soils Found.* 57 (4): 575–586. https://doi.org/10.1016/j.sandf.2017.03.009.

Zhang, L., Q. Ou, and M. Zhao. 2018. "Double-beam model to analyze the performance of a pavement structure on geocell-reinforced embankment." *J. Eng. Mech.* 4 (8): 06018002. https://doi.org/10.1061/(ASCE)EM.1943-7889.0001453.

Zhang, L., B. Peng, Z. Xu, and S. Zhou. 2022. "Shear performance of geosynthetic-encased stone column based on 3D-DEM simulation." *Comput. Geotech.* 151 (Nov): 104952. https://doi.org/10.1016/j.compgeo.2022.104952.